Analytica Chimica Acta 1082 (2019) 152–164

Contents lists available at ScienceDirect

Analytica Chimica Acta

journal homepage: www.elsevier.com/locate/aca

Recyclable metal nanoparticle-immobilized polymer dot on montmorillonite for alkaline phosphatase-based colorimetric sensor with photothermal ablation of Bacteria

Akhmad Irhas Robby [a], Sung Young Park [a, b, *]

[a] Department of IT Convergence, Korea National University of Transportation, Chungju, 380-702, Republic of Korea
[b] Department of Chemical and Biological Engineering, Korea National University of Transportation, Chungju, 380-702, Republic of Korea

HIGHLIGHTS

- Reusable material was designed for fluorometric sensing and photothermolysis of bacteria.
- The fluorescence ON/OFF sensing system was depended on the bacterial ALP activity.
- The LOD of fluorescence-based bacteria detection showed below 10^1 CFU/mL.
- Hybrid nanocomposite showed ±100% killing efficiency after 5 min NIR irradiation.
- Antibacterial/bacteria sensing showed excellent performance even after 4 cycles.

GRAPHICAL ABSTRACT

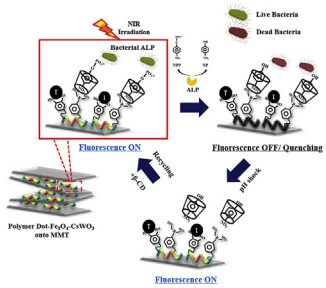

ARTICLE INFO

Article history:
Received 16 May 2019
Received in revised form
11 July 2019
Accepted 24 July 2019
Available online 27 July 2019

Keywords:
Alkaline phosphatase
Polymer dot
Montmorillonite
Iron oxide
Cesium tungsten oxide
Colorimetric detection

ABSTRACT

Development of simultaneous bacteria detection and eradication with simple, rapid, and reusable material is important in addressing bacterial contamination issues. In this study, we utilized the expression of alkaline phosphatase (ALP) from bacteria to design fluorescence ON/OFF system for bacteria detection, also using metal oxide nanoparticle for obtaining antibacterial activity and recyclability. The fluorescent-based biosensor with antibacterial activity was prepared by intercalating ALP-sensitive polymer dot (PD) containing β-cyclodextrin (β-CD) onto montmorillonite (MMT) as loading matrix *via* ionic exchange reaction, followed by immobilization of magnetic iron oxide (Fe_3O_4) and NIR-responsive cesium tungsten oxide ($CsWO_3$). The PD-βCD-MMT/Fe_3O_4–$CsWO_3$ nanocomposite exhibited strong fluorescence intensity, which was quenched in the presence of bacterial ALP (0–1000 U/L) due to hydrolysis of *p*-nitrophenyl phosphate (NPP) into *p*-nitrophenol (NP) in the hydrophobic site of β-CD. Furthermore, the nanocomposite could detect both gram-negative *Escherichia coli* and gram-positive *Staphylococcus aureus* in the range of 10^1–10^7 CFU/mL (LOD 5.09 and 4.62 CFU/mL, respectively), and showed high antibacterial activity against bacteria by generating photothermal heat under 5 min NIR irradiation, causing damage to bacterial cells. This material also demonstrated recyclability *via* magnetic field exposure due to the presence of Fe_3O_4. In addition, the fluorescence can be recovered following pH shock and re-conjugation of β-CD molecules. After 4 cycles, nanocomposite still showed stable photothermal effects and

* Corresponding author. Department of IT Convergence, Korea National University of Transportation, Chungju, 380-702, Republic of Korea.
E-mail address: parkchem@ut.ac.kr (S.Y. Park).

https://doi.org/10.1016/j.aca.2019.07.053

fluorescence-based bacteria detection. Thus, this reusable material offers promising approach for simultaneous bacteria detection and killing, which is simple, rapid, and effective.

1. Introduction

Pathogenic bacterial contamination is considered a major health issue due to its substantial impact on human health [1,2]. Various infectious diseases, such as tuberculosis and pneumonia, are associated with bacterial contamination, which spreads easily through direct contact, water contamination, and air pollution [3,4]. Much research is focused on the development of biosensors to detect bacteria in order to replace conventional methods, such as plate culturing, ELISA, and PCR which are time-consuming, require specialized instruments, and need specific chemical treatments to achieve high sensitivity [5–8]. However, there are still a few reports regarding recyclable material which combine bacteria-sensing ability with antibacterial activity for synergistic detection and eradication of bacteria. By combining biosensing techniques with antibacterial effects, efficient action can be taken simultaneously to rapidly diagnose and prevent bacterial contamination. Moreover, recyclable properties of the material can reduce waste via reuse, making the material more efficient. Therefore, designing such a combination was felt to be intriguing due to its usefulness and applicability in efficient bacterial detection and eradication.

Our previous work had constructed antibacterial nanocomposites by immobilizing tungsten oxide ($CsWO_3$) and iron oxide (Fe_3O_4) nanoparticle into exfoliated montmorillonite clay (MMT) [9]. We introduced immobilization technology for metal nanoparticles by utilizing the interaction between catechol-functionalized polymer and metal nanoparticles in base condition. This hybrid nanocomposite-intercalated MMT showed excellent antibacterial activity due to photothermal effect of $CsWO_3$ with good stability in solution state. This nanocomposite also demonstrated recyclability under external magnetic field due to the presence of Fe_3O_4, resulting an efficient and less-waste antibacterial agent. In addition, by intercalating active polymer material into the silicate layer of MMT clay, they showed good thermal stability compared to active polymer only and potentially provided good active site for bacteria detection due to its surface area. In our view, combining this material with biosensor such as polymer dot (PD) [10–12] may become a promising strategy to design a nanocomposite for reusable bacteria detection with excellent antibacterial activity.

Alkaline phosphatase (ALP) is an essential enzyme which is widely distributed in organs, tissues, and also expressed in gram-positive and gram-negative bacteria [13–17]. ALP is commonly known as an indicator of various diseases such as bone tumor and breast cancer [18,19]. ALP can hydrolyze various phosphate substrates, for example *p*-nitrophenyl phosphate (NPP) into *p*-nitrophenol (NP) [20–22], and this phenomenon had been utilized for developing fluorescence-based sensor [23–26]. For example, our previous work was designing fluorescence-based techniques using β-cyclodextrin (β-CD)-functionalized fluorescent nanoparticles [27]. By utilizing host-guest recognition of NPP in the cavity of β-CD, the ALP will hydrolyze NPP into NP and cause photo-induced electron transfer (PET). This PET phenomenon leads to the diminishing of fluorescence intensity which is correlated with the concentration of ALP. However, this method and some other works were developed for cancer cell detection. There are still a few reports about fluorescence-based bacteria sensor which utilize the expression of bacterial ALP. Therefore, by utilizing the expression of ALP from bacteria towards phosphate substances, the enzymatic fluorescence-based bacteria sensor can be developed. Furthermore, there are no reported studies combining enzymatic-responsive bacterial detection with antibacterial activity and recyclable properties. Hence, it may be useful to develop a simple, effective and reusable method by designing recyclable material for simultaneous detection and eradication of bacteria.

In this report, we designed a recyclable nanocomposite for the detection and eradication of bacteria based on bacterial ALP expression and photothermolysis of bacteria. An ALP-sensitive PD containing β-CD was intercalated onto MMT as a loading matrix *via* ionic exchange reaction [9,28,29], followed by immobilization of $CsWO_3$ and Fe_3O_4 *via* metal-catecholate interaction [9]. The sensing mechanism was relied on fluorescence on/off system between ALP-sensitive PD and bacteria, which bacteria expressed ALP to hydrolyze NPP into NP in the cavity of β-CD and caused fluorescence quenching due to the occurrence of PET phenomenon. Furthermore, this nanocomposite was able to generate photothermal heat under NIR irradiation due to the presence of $CsWO_3$, which triggered the photothermolysis of bacterial cells. In addition, due to the presence Fe_3O_4, the nanocomposite can be recycled under external magnetic field and further can be reused after re-conjugating β-CD molecules into the nanocomposite. Thus, this reusable material offers promising strategy for simultaneous detection and eradication of bacteria with a simple, rapid, and effective approach.

2. Materials and methods

2.1. Materials

Polyethylene glycol (PEG, MW: 3500), 2-(dimethylamino) ethyl methacrylate (DMA), *t*-butyl peroxybenzoate, bromoethane, 2-chloro-3′,4′-dihydroxyacetophenone (CCDP), 4-chlorophenylboronic acid, montmorillonite (MMT), β-cyclodextrin (β-CD), *p*-Nitrophenyl phosphate (NPP), Iron (II,III) oxide (Fe_3O_4) nanoparticle (50–100 nm), ALP inhibitor sodium metavanadate (Na_3VO_4), sulfuric acid (H_2SO_4), ethanol, tetrahydrofuran (THF), hexane, diethyl ether, deionized water (DDW), phosphate-buffer saline (PBS), 3-(4,5-dimethylthiazol-2-yl)-2,5-diphenylterazolium bromide (MTT), MRS and Luria-Bertani media were purchased from Sigma-Aldrich, South Korea. NIR-responsive $Cs_{0.33}WO_3$ nanoparticle ($CsWO_3$) was synthesized using a previously described method [30]. Propidium iodide (PI) and SYTO 9 were purchased from Molecular Probes, Life Technologies (Invitrogen, South Korea).

2.2. Characterizations

^{1}H NMR spectra were acquired using a Bruker AVANCE 400 MHz spectrometer. The UV–vis–NIR spectra were recorded with a UV–vis absorption spectrometer (Optizen 2120 UV spectrophotometer, Mecasys). X-ray diffraction spectra were observed using an XRD Bruker AXS ADVANCES D-8. Dynamic light scattering (DLS; Zetasizer Nano, Malvern, Germany) was used to measure particle size. Magnetic properties of sample were recorded using alternating gradient magnetometer (AGM; 2900-02). The fluorescence

profiles were determined using a luminescence spectrometer (L550B, PerkinElmer). The NIR laser was 808 nm (PSU-III-LRD, CNI Optoelectronics Tech. Co. LTD, China). A confocal laser scanning microscope (CLSM; LSM510 Carl Zeiss, Germany) was used to observe live and dead bacteria with 488 and 543 nm emission filters. Flow cytometric analysis (FACS) was conducted using an Attune NxT Acoustic Focusing Cytometer. Scanning electron microscopy (SEM) was performed with a JSM-6700F, JEOL (Japan). Photo-thermal heating curves were examined using an infrared camera (NEC Avio, Thermo Tracer TH9100). Identification and quantification of metal components was performed by measurement *via* inductively coupled plasma mass spectrometry (ICP-MS) (Bruker 820-MS, Germany).

2.3. Synthesis of $CsWO_3$

Briefly, ammonium tungstate ($(NH_4)_{10}H_2(W_2O_7)_6$), ammonium molybdate ($H_8MoN_2O_4$) and cesium carbonate (Cs_2CO_3) were mixed in DDW and stirred at room temperature for 1 h. The solution was further heated at 180 °C for 8 h. The resulted powder was annealed in vacuum furnace at 500 °C for 1 h under nitrogen atmosphere [30].

2.4. Synthesis of boronic acid-conjugated CA-g-PEG-g-PDMA (B/C-PgP)

The catechol-conjugated polyethylene glycol-grafted poly(-dimethylamino)ethyl methacrylate (CA-g-PEG-g-PDMA) was prepared according to a previously published method [31], which the obtained amount of catechol moieties in CA-g-PEG-g-PDMA (degree of quaternization) was 18 units based on calculation from ^{1}H NMR spectra analysis between peak area of aromatic catechol at 7.4 ppm compared to peak area of PEG at 3.7 ppm. To provide a sufficiently high positive charge for MMT intercalation *via* ionic exchange, CA-g-PEG-g-PDMA was modified with bromoethane *via* quaternization reaction. In brief, 0.25 mmol of CA-g-PEG-g-PDMA and 3.72 mmol of bromoethane was dissolved in 150 mL anhydrous ethanol and stirred under nitrogen atmosphere for 24 h at 70–80 °C. The solution was then evaporated using a rotary evaporator and precipitated in diethyl ether. Finally, the precipitate was dried in a vacuum oven. Quaternary ammonium that resulted from this reaction was estimated to be approximately 153 units based on calculation from ^{1}H NMR spectra analysis between peak area of bromoethane at 3.4 ppm compared to peak area of PEG at 3.7 ppm.

To synthesize boronic acid-conjugated CA-g-PEG-g-PDMA (B/C-PgP), 4-chlorophenyl boronic acid (0.03 mmol) and CA-g-PEG-g-PDMA (0.99 mmol) were mixed with 150 mL anhydrous ethanol and allowed to react for 24 h at 70–80 °C while stirring under a nitrogen atmosphere. The solution was evaporated in a rotary evaporator and precipitated in diethyl ether. The resulting precipitate of B/C-PgP was then dried in vacuum oven. The boronic acid moieties in B/C-PgP were estimated to be 26 units based on calculation from ^{1}H NMR spectra analysis between peak area of aromatic boronic acid at 7.2 ppm compared to peak area of PEG at 3.7 ppm.

2.5. Synthesis of polymer dot (PD) from B/C-PgP by carbonization method

PD was synthesized *via* carbonization of the B/C-PgP polymer using a strong acid (H_2SO_4) [32]. B/C-PgP was carbonized by dissolving 1 g polymer in 10 mL H_2SO_4 (36 N) for approximately 1 min. The purification process was conducted using dialysis (molecular weight cut-off = 1000) for 24 h against water, followed by freeze-drying to obtain the PD.

2.6. Intercalation of PD into montmorillonite (MMT)

PD was intercalated into MMT *via* ionic exchange reaction, as described in previously published studies [28,29]. Firstly, 0.95 g of PD was dissolved in a co-solvent of DDW (120 mL, pH 5) and ethanol (30 mL). MMT was dispersed in 120 mL of DDW and added to the previously prepared PD solution. This mixture was then stirred at 80 °C for 1 h, and the precipitate was filtered. Next, the precipitate was re-dispersed in 300 mL of water-ethanol solvent (volume ratio 1:1) and stirred for 1 h. The final product (PD-MMT) then was filtrated and placed in the freeze dryer.

2.7. Immobilization of iron oxide (Fe_3O_4) and tungsten oxide ($CsWO_3$) onto PD-MMT

The immobilization of Fe_3O_4 and $CsWO_3$ onto PD-MMT was relied on the metal-catecholate coordination between metal oxide nanoparticle and catechol moieties which were present in PD-MMT. First, the 5 mL dispersion of Fe_3O_4 nanopowder (0.01 g) in THF was carefully added to the 30 mL dispersion of PD-MMT (0.1 g) in ethanol. The mixture was stirred using a mechanical stirrer for 24 h at room temperature. After reaction, the mixture was placed in a rotary evaporator in order to evaporate the solvent, and the remaining sample was precipitated using hexane. The precipitate was then centrifuged and freeze dried to obtain the PD-MMT/Fe_3O_4 pellet. To conduct $CsWO_3$ immobilization, the $CsWO_3$ nanoparticle and PD-MMT/Fe_3O_4, at a weight ratio of 1:20, were dispersed in PBS solution (pH 8,5). The dispersion was stirred using a mechanical stirrer for 24 h at room temperature, and then centrifuged and freeze dried to obtain the PD-MMT/Fe_3O_4–$CsWO_3$ pellet.

2.8. Conjugation of β-cyclodextrin (β-CD) into PD-MMT/Fe_3O_4–$CsWO_3$

The mechanism for β-CD conjugation was relied on diol-diol interaction between β-CD and boronic acid in PD which can be activated in base condition. However, pH shock at acid condition was necessary as a pretreatment to prevent early diol-diol cross-linking between each boronic acid and catechol of CCDP with boronic acid, which can potentially block the β-CD conjugation. Fig. S1 showed that by using pH 6 before β-CD conjugation, the nanocomposite can be used for ALP-sensitive sensor indicated by fluorescence quenching in the presence of NPP and ALP. Otherwise, MMT-intercalated nanocomposite did not show significant fluorescence quenching when pH 7.4 or above were used for pH shock. Therefore, we did a pH shock at pH 6 before β-CD conjugation and followed by β-CD conjugation at pH 12.

Firstly, PD-MMT/Fe_3O_4–$CsWO_3$ was dispersed in PBS pH 6.0 (pH shock) for 1 h, then centrifuged and filtered. Subsequently, PD-MMT/Fe_3O_4–$CsWO_3$ and β-CD (weight ratio 1:1) were dissolved in PBS pH 12 and allowed to react for 24 h at room temperature. Finally, the mixture was centrifuged and freeze dried to obtain the PD-βCD-MMT/Fe_3O_4–$CsWO_3$ pellet.

2.9. Fluorescent quenching of PD-βCD-MMT/Fe_3O_4–$CsWO_3$ in the presence of NPP and ALP

45 μL of NPP solution (10 mM) and 10 μL of $MgSO_4$ solution (0.1 μM) were added to PD-βCD-MMT/Fe_3O_4–$CsWO_3$ solution (1 mg/mL in TBS pH 7.4). Subsequently, 10 μL of ALP in various concentrations (0–1000 U/L) was added to the solution and incubated in a shaking incubator for 15 min at 37 °C. The fluorescent spectra of each solution containing ALP were recorded using PL spectroscopy at an excitation wavelength of 440 nm.

2.10. Sensing of bacteria by PD-βCD-MMT/Fe_3O_4–$CsWO_3$ based on fluorescence assay

A bacterial solution containing *E. coli* and *S. aureus* (10^1–10^7 CFU/mL) was prepared using LB and MRS media, respectively. The PD-βCD-MMT/Fe_3O_4–$CsWO_3$ (1 mg/mL) containing NPP (10 mM) and $MgSO_4$ (0.1 μM) was added to the prepared bacterial solution, followed by 15 min incubation at 37 °C in shaking incubator. After incubation, the bacterial solutions containing PD-βCD-MMT/Fe_3O_4–$CsWO_3$ were centrifuged for 5 min, followed by washing the obtained pellet with PBS three times. The obtained bacteria-labeled PD-βCD-MMT/Fe_3O_4–$CsWO_3$ pellet was dissolved in 1 mL of PBS pH 7.4, and its fluorescent emission was analyzed using a PL spectrometer, a flow cytometer and a confocal laser scanning microscope. The PD-βCD-MMT/Fe_3O_4–$CsWO_3$ solution alone was used as a control. To observe the role of bacterial ALP in bacterial detection, an ALP inhibitor (1 mg/mL of Na_3VO_4) was added to the bacterial solution and analyzed using the same steps described above.

2.11. Live and dead bacteria killing assay

Solutions of *E. coli* and *S. aureus* (10^7 CFU/mL) containing various concentrations of PD-βCD-MMT/Fe_3O_4–$CsWO_3$ (0.1–1 mg/mL) were irradiated with 808 nm NIR laser (laser power 2 W/cm^2) for 5 min. The bacterial cell viability was then evaluated via MTT assay with the bacterial solution alone as the control. To estimate live and dead bacteria, confocal laser scanning microscopy and flow cytometry analysis were conducted using SYTO 9 (live) and PI staining (dead).

2.12. Recyclability of PD-βCD-MMT/Fe_3O_4–$CsWO_3$ for reusable detection and killing of bacteria

After detecting and killing bacteria, the used PD-βCD-MMT/Fe_3O_4–$CsWO_3$ was separated from the sample using a magnetic bar and dissolved in PBS pH 6.0 (pH shock) to cleave the diol-diol bond between boronic acid and β-CD. After 1 h, the solution was centrifuged to obtain the pellet (PD-MMT/Fe_3O_4–$CsWO_3$) which was recycled for future use. In order to reuse the material, the obtained pellet and β-CD were dissolved in PBS pH 12 and allowed to react for 24 h in room temperature. Subsequently, this mixture was centrifuged and freeze dried to obtain fresh PD-βCD-MMT/Fe_3O_4–$CsWO_3$.

3. Results and discussion

3.1. Material design, sensing mechanism and concept of applications

Utilizing ALP-responsive polymer dot (PD), NIR-responsive $CsWO_3$, and Fe_3O_4 nanoparticle, we designed a material capable of simultaneous detection and eradication of bacteria, with a simple, effective, and recyclable system. PD-βCD-MMT/Fe_3O_4–$CsWO_3$ was synthesized by intercalating the PD onto MMT clay, followed by immobilization of $CsWO_3$ and Fe_3O_4 (Scheme 1a). The cation in MMT layer can be easily exchanged with another cation such as a cationic polymer, which makes it possible to exfoliate this clay using various cationic polymers [33,34]. Due to this advantage, cationic PD can be intercalated onto MMT *via* ionic exchange reaction due to the presence of quaternary ammonium in the PD backbone. The quaternary ammonium in PD provided enough positive charge to displace the Na^+ in the silicate interlayer, enabling PD to intercalate onto MMT. Following intercalation, Fe_3O_4 and $CsWO_3$ were immobilized onto PD-MMT *via* interaction between catechol moieties of PD and the metal nanoparticle. This interaction allowed Fe_3O_4 and $CsWO_3$ to remain stable on PD-MMT/Fe_3O_4–$CsWO_3$, as a result of which, this nanocomposite produced a photothermal effect under NIR irradiation and the magnetic properties required for a reusable antibacterial agent. To acquire bacteria-sensing ability, β-CD was conjugated to form PD-βCD-MMT/Fe_3O_4–$CsWO_3$ under basic conditions (pH 12). This conjugation was possible due to the diol-diol interaction between the diol groups of boronic acid in PD and the diol groups of β-CD [35]. In this system, β-CD played a key role in detecting bacteria based on a fluorometric assay. β-CD promotes a host-guest interaction with NPP, and upon hydrolysis of NPP by ALP into NP, photo-induced electron transfer (PET) occurred, causing fluorescence quenching of PD [26,27].

The reusable platform for detection and eradication of bacteria is shown (Scheme 1b). PD-βCD-MMT/Fe_3O_4–$CsWO_3$ was introduced into the bacteria-contaminated solution, and the fluorescence of PD-βCD-MMT/Fe_3O_4–$CsWO_3$ diminished due to the hydrolysis of NPP by bacterial ALP. Moreover, when the solution was irradiated using a NIR laser, PD-βCD-MMT/Fe_3O_4–$CsWO_3$ generated heat that triggered photothermolysis causing damage to the bacterial cell. Following application, PD-βCD-MMT/Fe_3O_4–$CsWO_3$ may be reused by introducing a magnetic field, resulting in the separation of material from the solution. By conducting pH shock and re-conjugation of β-CD, the fluorescent intensity of recycled material may be recovered and applied for further use.

3.2. Structural characterizations

Structural characterization was conducted to determine the chemical structure of PD-βCD-MMT/Fe_3O_4–$CsWO_3$. As shown by ^{1}H NMR data, peaks of 0.8 [3H, $-CH_3$], 1.0 [2H, $-CH_2$-], 2.5 [3H, $-CH_3$-N], 3.5 [2H, N–CH_2] 3.7 [PEG], 4.2 [2H, $-CH_2$-N], validated the PEG-g-PDMA polymer backbone (Fig. 1a). Furthermore, the integral peak at 6.7–7.5 referred to the aromatic compounds of boronic acid and catechol moieties, indicating successful quaternization of boronic acid and the catechol group [31,35,36]. UV–visible spectrometry was also conducted (Fig. 1b). A strong absorption peak at 235 nm and a weak absorption peak at 290 nm were observed, confirming the presence of boronic acid in the material. An absorption peak which appeared at 360 nm corresponds to the π-π transition of aromatic compounds in catechol groups [35]. To further assess the intercalation of PD onto MMT and immobilization of Fe_3O_4 and $CsWO_3$, x-ray diffraction analysis (XRD) was conducted. This revealed a significant diffraction pattern change in 2θ value of pure MMT at 7° before and after intercalation of PD (Fig. 1c). Before intercalation, pure MMT showed d-space at 7°, which disappeared when PD was intercalated onto MMT. Thus, this data revealed the successful intercalation of PD onto MMT, resulting from ionic interaction between the positive charge of PD with the negative charge in the silicate interlayer of MMT [9,28,29]. Further, XRD results showed a diffraction pattern of 10° and between 20 and 60°, indicating the presence of β-CD and successful immobilization of Fe_3O_4 and $CsWO_3$ nanoparticles, respectively (Fig. 1d). FT-IR analysis was performed to determine the chemical structure of PD-βCD-MMT/Fe_3O_4–$CsWO_3$. The stretching peak of Si–O in MMT at 1050 cm^{-1}, C–H stretching of PD at 2800-2900 cm^{-1}, –OH stretching of PD at 3400 cm^{-1}, C=O stretching at 1680 -1750 cm^{-1}, B–O stretching at 1350 cm^{-1}, W–O stretching at 620 cm^{-1}, and Fe–O stretching at 462 cm^{-1} were detected, confirming the structure as PD-βCD-MMT/Fe_3O_4–$CsWO_3$ (Fig. S2).

DLS measurement in aqueous solution (0.001 mg/mL) was conducted in order to analyze the size distribution of PD-βCD-MMT/Fe_3O_4–$CsWO_3$. The average particle size of PD, which was

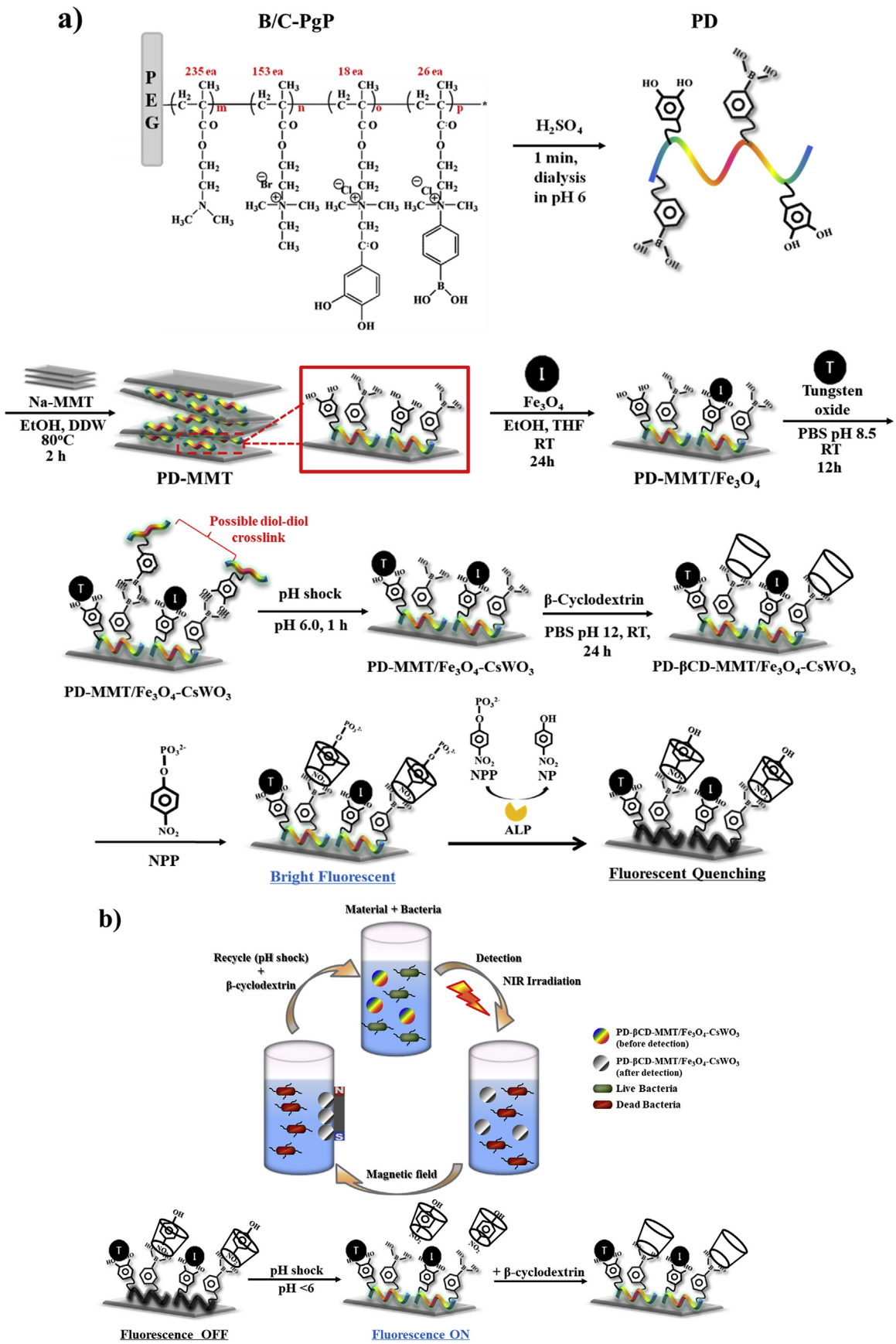

Scheme 1. (a) Illustration of intercalation of ALP-responsive PD onto montmorillonite (MMT) and immobilization of Fe_3O_4 and $CsWO_3$. (b) Application of PD-βCD-MMT/Fe_3O_4–$CsWO_3$ for reusable detection and eradication of bacteria.

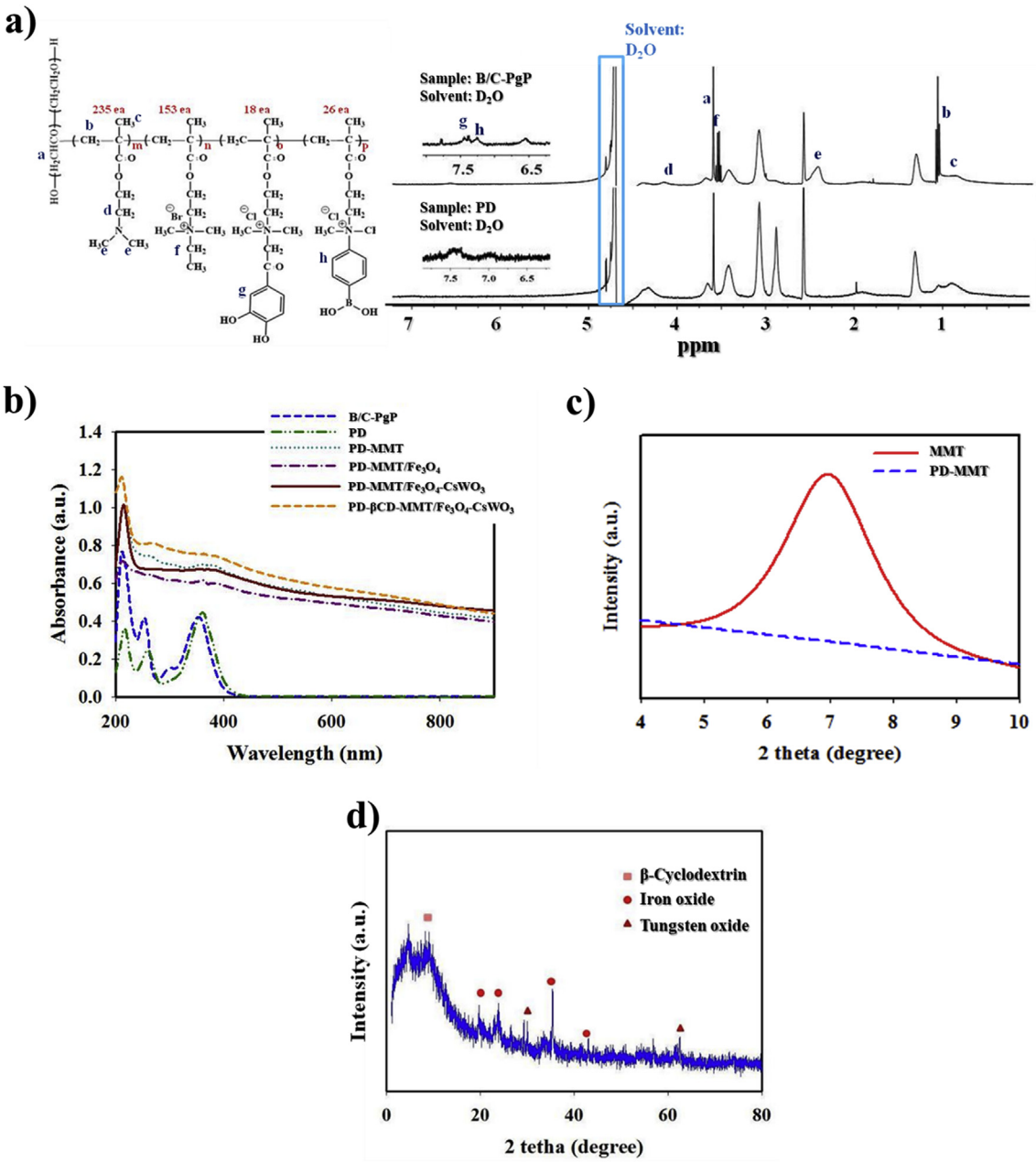

Fig. 1. (a) H NMR spectra of B/C-PgP and PD in D_2O. (b) UV–Visible spectrum in aqueous solution (0.1 mg/mL). (c) XRD patterns of MMT and PD-MMT in the 2θ range of 4–10°. (d) XRD patterns of PD-βCD-MMT/Fe_3O_4–$CsWO_3$ in the 2θ range of 1–80°.

14.8 nm, increased following intercalation and immobilization, up to the average diameter of PD-βCD-MMT/Fe_3O_4–$CsWO_3$, which was 264.5 nm (Fig. 2a). Furthermore, to examine the effect of Fe_3O_4 nanoparticle immobilization on the magnetic property of material, an alternating gradient magnetometer was used to characterize its magnetic properties. After immobilization of the Fe_3O_4 nanoparticle, PD-βCD-MMT/Fe_3O_4–$CsWO_3$ showed strong magnetic properties, as magnetization was enhanced when the material was exposed to a magnetic field (Fig. 2b). This phenomenon was also confirmed by testing the magnetic properties of PD-βCD-MMT/Fe_3O_4–$CsWO_3$ by external magnet exposure on the PD-βCD-MMT/Fe_3O_4–$CsWO_3$ solution. PD-βCD-MMT/Fe_3O_4–$CsWO_3$ was responsive to the magnetic stimulus as the material, which was attracted to the magnetic pole, separated from the solution (Fig. 2c). When magnetic exposure was diminished, the PD-βCD-MMT/Fe_3O_4–$CsWO_3$ particle returned to its normal condition with recovery rate was above 95%. These results proved that the Fe_3O_4 nanoparticle was successfully immobilized to the nanocomposite, allowing separation from solution *via* magnetic exposure which is useful for recycling the material. This was also confirmed by TEM images at Fig. S3. The TEM images revealed the immobilization process of metal oxide nanoparticle including Fe_3O_4 and $CsWO_3$. The TEM images of PD-βCD-MMT/Fe_3O_4–$CsWO_3$ showed the lattice structure of PD (d-spacing = 0.31–0.33 nm), Fe_3O_4 (d-spacing = 0.26 nm) and $CsWO_3$ (d-spacing = 0.36–0.37 nm) which indicated successful immobilization of metal oxide nanoparticle into PD-MMT.

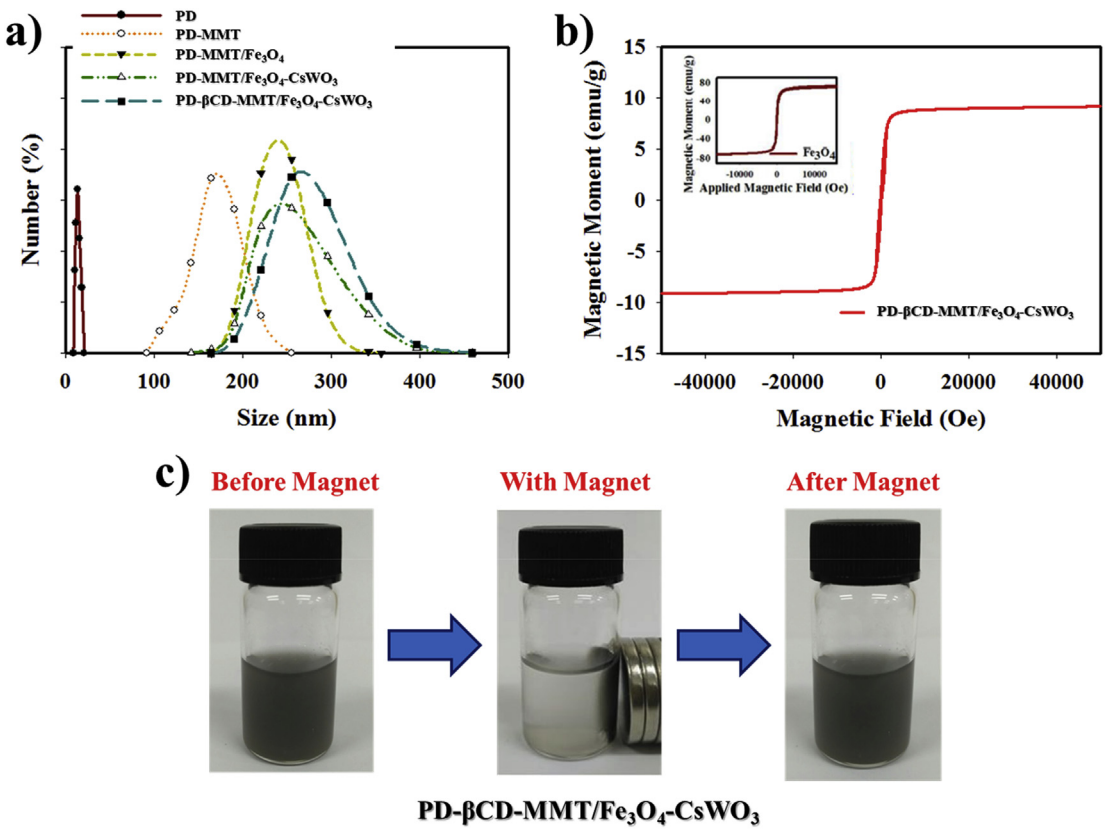

Fig. 2. (a) Particle size measurement based on DLS in aqueous solution (0.001 mg/mL). (b) Magnetization curve of Fe_3O_4 (inset) and PD-βCD-MMT/Fe_3O_4–$CsWO_3$. (c) Photograph of the magnetic effect of PD-βCD-MMT/Fe_3O_4–$CsWO_3$ in water (1 mg/mL).

3.3. Bacteria detection assay

Bacterial detection was reliant upon the fluorescent change of PD-βCD-MMT/Fe_3O_4–$CsWO_3$ due to bacterial ALP activity. The fluorescence behavior of PD-βCD-MMT/Fe_3O_4–$CsWO_3$ was assessed using PL spectroscopy analysis. Firstly, all excitation-dependent PL spectra of each process were determined in 1 mg/mL of material solution as shown in Fig. S4. Based on these data, PD itself showed high fluorescence intensity with highest intensity (28000 a.u.) was at excitation wavelength of 380 nm. When PD was intercalated into MMT, PD-MMT also showed highest fluorescence intensity (26000 a.u.) at excitation wavelength of 380 nm. However, the highest fluorescence intensity was shifting into excitation wavelength of 440 nm and dramatically increasing (58000–61000 a.u.) after immobilization of Fe_3O_4 and $CsWO_3$. The shifting and enhancement of fluorescence intensity was possibly due to surface plasmon resonance of Fe_3O_4 and $CsWO_3$ which was overlapped with broad fluorescence spectrum of polymer dot [37–39]. Therefore, we use excitation wavelength of 440 nm as an experimental condition for determining sensing performance of PD-βCD-MMT/Fe_3O_4–$CsWO_3$, with initial fluorescence intensity was showed in Fig. 3a. The PD-βCD-MMT/Fe_3O_4–$CsWO_3$ also showed fluorescence stability in various environments such as temperature and salt-containing water as shown in Fig. S5. To examine the effect of ALP activity on fluorescence of the material, the PD-βCD-MMT/Fe_3O_4–$CsWO_3$ was mixed with NPP solution (10 mM) and various concentrations of ALP (0–1000 U/L), and the resulting fluorescent intensity was checked under a PL spectrometer, revealing a gradual decrease in fluorescent intensity with increasing ALP concentration (Fig. 3b). Fluorescent quenching was initiated when ALP concentration increased to reach 10 U/L and complete quenching occurred when the ALP concentration reached 500 U/L. The fluorescent quenching mechanism of PD-βCD-MMT/Fe_3O_4–$CsWO_3$ was depended on the PET phenomenon promoted by a host-guest interaction between β-CD in the nanocomposite and NP [26,27]. First, NPP enters the hydrophobic site of β-CD *via* a hydrophobic interaction between the aromatic ring of NPP and the hydrophobic site inside β-CD. When the ALP present in the solution, ALP will hydrolyze the NPP into NP and initiates the PET phenomenon, resulting in the diminishing of fluorescent emission intensity. To further understand the role of host-guest interaction on the quenching mechanism, the fluorescence of nanocomposite with and without β-CD (PD-MMT/Fe_3O_4–$CsWO_3$) was observed in the presence of NPP (10 mM) and ALP (1000 U/L) (Fig. S6). As can be seen in Fig. S6a, both nanocomposites exhibited high fluorescence intensity before the addition of NPP and ALP. However, the nanocomposite without β-CD did not show significant quenching compared with β-CD-conjugated nanocomposite in the presence of NPP and ALP (Fig. S6b). This understandably was due to no PET phenomenon occurred as a result of unavailability of host-guest interaction between NP and β-CD in the nanocomposite. In addition, to confirm the role of NP as a PD-βCD-MMT/Fe_3O_4–$CsWO_3$ fluorescence quencher, PL spectroscopy analysis was conducted on PD-βCD-MMT/Fe_3O_4–$CsWO_3$ solution in the presence of various concentrations of NP (0–10 mM). Results showed that the fluorescence intensity of PD-βCD-MMT/Fe_3O_4–$CsWO_3$ was quenched at higher NP concentrations (Fig. S7). This result confirmed that the presence of NP in the cavity of βCD resulted in fluorescent quenching in PD-βCD-MMT/Fe_3O_4–$CsWO_3$.

To verify bacteria-sensing efficacy, the PD-βCD-MMT/Fe_3O_4–$CsWO_3$ was applied to a pathogenic bacteria solution, containing *E. coli* (gram-negative bacteria) and *S. aureus* (gram-positive

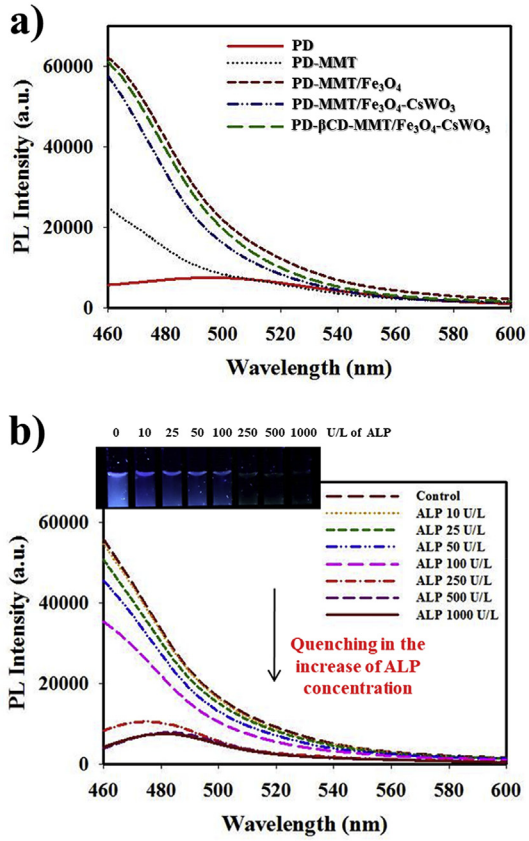

Fig. 3. (a) PL spectra of material at excitation wavelength of 440 nm (1 mg/mL in TBS 7.4). (b) Quenching effect of PD-βCD-MMT/Fe_3O_4–$CsWO_3$ due to NPP hydrolysis in the presence of various ALP concentrations. Control was 1 mg/mL of PD-βCD-MMT/Fe_3O_4–$CsWO_3$ without ALP.

bacteria). First, each *E. coli* and *S. aureus* solution (10^7 CFU/mL) was treated with various concentrations of PD-βCD-MMT/Fe_3O_4–$CsWO_3$ (0.1–1 mg/mL) containing NPP (10 mM). The fluorescence intensity was checked following shaking incubation for 15 min at 37 °C. Compared to the control of untreated bacterial solution, the fluorescence intensities of material-treated bacteria were significantly quenched in all PD-βCD-MMT/Fe_3O_4–$CsWO_3$ concentrations for both *E. coli* and *S. aureus* (Fig. 4a and b). Further evaluation was conducted by treating various *E. coli* and *S. aureus* concentrations (10^1–10^7 CFU/mL) with fixed PD-βCD-MMT/Fe_3O_4–$CsWO_3$ solution concentrations (1 mg/mL) containing NPP (10 mM). After incubation for 15 min at 37 °C, the fluorescence intensities were remarkably quenched in the range of 10^1–10^7 CFU/mL in *E. coli* and *S. aureus* solutions, compared with the control PD-βCD-MMT/Fe_3O_4–$CsWO_3$ solution (1 mg/mL) (Fig. 4c and d). The calibration curve in Fig. S8 further showed linearity of fluorescence quenching in the wide range of bacteria concentration (10^1–10^8 CFU/mL), with regression (R^2) were above 0.999 and limit of detection (LOD) were 5.25 CFU/mL for *E. coli* and 5.45 CFU/mL for *S. aureus*. This result revealed that the nanocomposite showed remarkable sensitivity towards gram-positive and gram-negative bacteria up to below than 10^1 CFU/mL. For comparison, the obtained LOD value of this system was compared with recent bacteria detection methods, including fluorescence-, SPR- and light scattering-based assay [40–45]. As can be seen in Table S1, this system showed lower LOD value compared to recent method which indicated better sensitivity for bacteria detection. Therefore, this method can be applied as a potential bacteria biosensor with more sensitivity towards both gram-positive and gram-negative bacteria. Fluorescence quenching of PD-βCD-MMT/Fe_3O_4–$CsWO_3$ in bacterial solutions was further confirmed under confocal laser scanning microscopy and flow cytometry analysis (FACS) [46]. The confocal image showed bright fluorescence in the absence of bacteria, whereas material treated with *E. coli* and *S. aureus* lost their fluorescence intensities (Fig. 4e). Under FACS analysis, mean fluorescence intensity of PD-βCD-MMT/Fe_3O_4–$CsWO_3$ was decreased from 216 (Fig. 5a) to 176 when treated with *E. coli* (Fig. 5b), and from 216 to 172 when treated with *S. aureus* (Fig. 5c) in the presence of NPP. These results demonstrated that bacteria may hydrolyze NPP into NP due to native bacterial ALP, resulting in the fluorescence quenching of PD-βCD-MMT/Fe_3O_4–$CsWO_3$. To confirm the role of bacterial ALP in the fluorescence quenching of PD-βCD-MMT/Fe_3O_4–$CsWO_3$, Na_3VO_4 solution (1 mg/mL) was introduced into the PD-βCD-MMT/Fe_3O_4–$CsWO_3$ and bacteria mixture. The fluorescent emission spectra of PD-βCD-MMT/Fe_3O_4–$CsWO_3$ (1 mg/mL) in the presence of ALP inhibitor Na_3VO_4 and various bacterial concentrations (10^1–10^7 CFU/mL) is shown (Fig. S9). The results indicated that fluorescence quenching did not occur in both *E. coli* and *S. aureus,* when Na_3VO_4 was present. Confocal laser scanning microscopy results further confirmed the effect of Na_3VO_4 in preventing the diminishing of fluorescent intensity (Fig. 4e). Furthermore, FACS data indicated that there was no significant change in fluorescence intensity between PD-βCD-MMT/Fe_3O_4–$CsWO_3$ treated with bacteria and Na_3VO_4, and PD-βCD-MMT/Fe_3O_4–$CsWO_3$ only as a control (Fig. S10). This demonstrated that bacterial ALP was unable to hydrolyze NPP due to inhibition of enzyme activity, suggesting the bacterial ALP may play a key role in fluorescence quenching of PD-βCD-MMT/Fe_3O_4–$CsWO_3$, and therefore may be utilized in fluorescence-based bacterial detection assays.

Considering the presence of coexisting substances in environmental sample which can interfere the result of detection, selectivity of nanocomposite on bacteria detection was further assessed in the presence of potential interferences including cationic (NH_4^+, Ca^{2+}, Zn^{2+}, Cu^{2+}) and anionic species (Cl^-, CO_3^{2-}, PO_4^{3-}, SO_4^{2-}). As can be seen in Fig. S11, each interference did not show any significant fluorescence quenching even after combined (soup). However, when bacteria were presence in combined interferences (bacteria + soup), the fluorescence intensity was dramatically quenched. Thus, this result revealed that PD-βCD-MMT/Fe_3O_4–$CsWO_3$ has excellent selectivity towards bacteria and expected can be applied in real environmental sample with coexisting interferences.

3.4. Determination of photothermal-based antibacterial activity

PD-βCD-MMT/Fe_3O_4–$CsWO_3$ was expected to be able to provide antibacterial activity under NIR irradiation due to the presence of NIR-responsive $CsWO_3$ in the system. Under NIR irradiation, PD-βCD-MMT/Fe_3O_4–$CsWO_3$ generated a photothermal effect which may cause photothermolysis of bacterial cells [9]. Temperature elevation at various PD-βCD-MMT/Fe_3O_4–$CsWO_3$ concentrations (0.1–1 mg/mL) after 5 min NIR irradiation is shown (Fig. 6a). The results revealed that the temperature increase was associated with irradiation time and PD-βCD-MMT/Fe_3O_4–$CsWO_3$ concentrations. When 1 mg/mL of PD-βCD-MMT/Fe_3O_4–$CsWO_3$ was irradiated with NIR laser for 5 min, the temperature rose about 27 °C, which is sufficiently high to damage bacterial cells. To assess antibacterial activity of PD-βCD-MMT/Fe_3O_4–$CsWO_3$, MTT assay was performed for *E. coli* and *S. aureus* at various PD-βCD-MMT/Fe_3O_4–$CsWO_3$ concentrations (0.1–1 mg/mL) under 5 min NIR irradiation. The bacteria cell viability of *E. coli* and *S. aureus* were also assessed using absence of NIR irradiation as a control. No significant decrease in

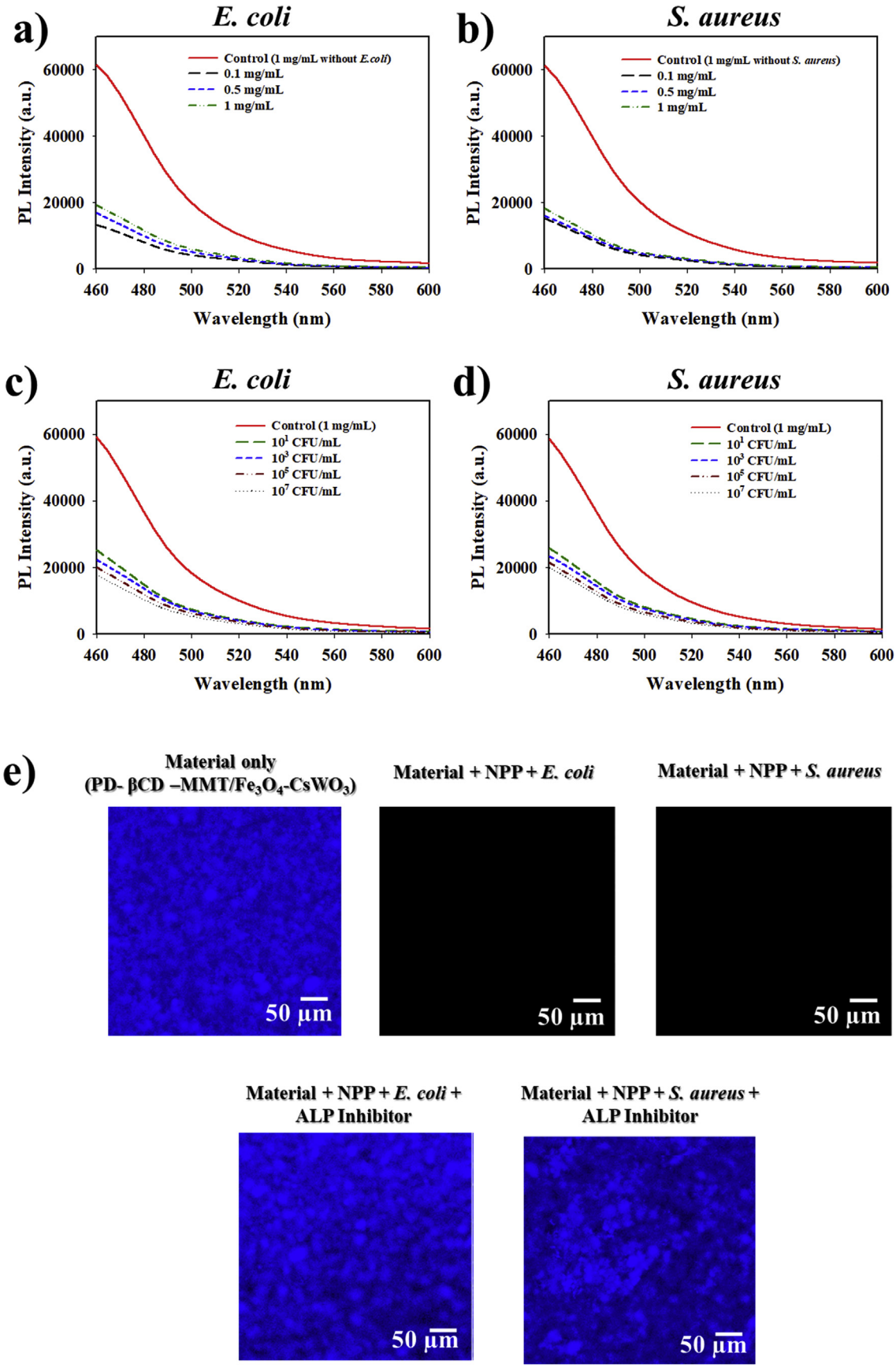

Fig. 4. PL spectra of various PD-βCD-MMT/Fe_3O_4–$CsWO_3$ concentrations (0.1–1 mg/mL) in the presence of (a) *E. coli* and (b) *S. aureus* with a fixed concentration of bacteria (10^7 CFU/mL), and PL spectra of PD-βCD-MMT/Fe_3O_4–$CsWO_3$ (1 mg/mL) in the presence of (c) *E. coli* and (d) *S. aureus* in various concentrations (10^1–10^7 CFU/mL). All experiments were conducted at an excitation wavelength of 440 nm. (e) Confocal images of PD-βCD-MMT/Fe_3O_4–$CsWO_3$ (1 mg/mL) treated with bacteria (10^7 CFU/mL) in the absence and presence of ALP inhibitor (1 mg/mL of Na_3VO_4).

bacteria cell viability was found in both *E. coli* and *S. aureus* when NIR irradiation was absent (Fig. 6b). By contrast, cell viability was significantly decreased in both *E. coli* and *S. aureus* when NIR irradiation was introduced, particularly at 1 mg/mL PD-βCD-MMT/Fe_3O_4–$CsWO_3$, where bacterial cell viability decreased almost a 100%. This result confirmed that NIR irradiation may enhance antibacterial activity of PD-βCD-MMT/Fe_3O_4–$CsWO_3$ by generating a photothermal effect. SEM imaging was conducted to visualize the damage to bacterial cells following NIR irradiation. As can be seen in Fig. 6(c), Both live *E. coli* and *S. aureus* bacterial cells, which had smooth surfaces before irradiation, lost their integrity after 5 min of NIR irradiation, resulting in death of these bacteria. The SEM images confirmed that the photothermal effect of PD-βCD-MMT/Fe_3O_4–$CsWO_3$ under NIR irradiation may damage bacterial cells, leading to the eradication of bacteria. Further testing for live and dead bacteria cells was performed using confocal laser scanning microscopy and FACS analysis, with SYTO 9 staining for live bacteria and PI staining for dead bacteria. Confocal images showed that both *E. coli* and *S. aureus* died after NIR exposure, as indicated by red color, whereas the bacteria without NIR exposure remained alive. as indicated by green color (Fig. 6d). Moreover, FACS data also indicated the live or dead status of bacteria after NIR irradiation, by the change in dot distribution, where the distribution moved from the lower quadrant (live/SYTO 9 staining) into the upper quadrant (dead/PI staining) (Fig. 6e) [47]. NIR irradiation of PD-βCD-MMT/Fe_3O_4–$CsWO_3$ caused *E. coli* & *S. aureus* viability to decrease by approximately 100%. Therefore, these results demonstrated the potential of PD-βCD-MMT/Fe_3O_4–$CsWO_3$ as an effective and efficient antibacterial agent when supplemented by NIR irradiation.

3.5. Real-world applications and recyclability of PD-βCD-MMT/Fe_3O_4–$CsWO_3$

To evaluate the bacteria sensing and antibacterial activity of material on real environment, contaminated river water from Dalcheon River, Chungju, South Korea was used as a real-world sample and treated with PD-βCD-MMT/Fe_3O_4–$CsWO_3$ and NPP. As can be seen in Fig. S12 (a and b), the fluorescence of PD-βCD-MMT/Fe_3O_4–$CsWO_3$ was quenched after treated with river water, contrary with DDW as a control. It confirmed that there was a presence of bacteria in the river water sample which can be sensitively detected by PD-βCD-MMT/Fe_3O_4–$CsWO_3$. Furthermore, the antibacterial activity was also observed under NIR irradiation depend on irradiation time. Fig. S12c showed that the bacteria killing efficiency in river water sample was increased depend on the irradiation time and reached around 100% with 5 min irradiation. Those results confirmed that PD-βCD-MMT/Fe_3O_4–$CsWO_3$ had excellent detection and bacteria killing performances on the real environmental sample.

PD-βCD-MMT/Fe_3O_4–$CsWO_3$ is a recyclable material for colorimetric sensor application, as it can be separated *via* a magnetic field and its fluorescence intensity can be recovered by pH shock and re-conjugating of new β-CD molecules onto PD-βCD-MMT/Fe_3O_4–$CsWO_3$. The recyclability of PD-βCD-MMT/Fe_3O_4–$CsWO_3$ as indicated by its performance after recycling was evaluated by observing temperature elevation and fluorescence intensity change before and after recycling. The temperature elevation of PD-βCD-MMT/Fe_3O_4–$CsWO_3$ under 5 min NIR irradiation remained stable after recycling 4 times, indicating the stability of $CsWO_3$ in the material (Fig. 7). This is due to the strong bond between metal nanoparticles such as Fe_3O_4 and $CsWO_3$ and the catechol moieties in the nanocomposite [9]. To prove the stability of metal nanoparticles in the nanocomposite, ICP-MS analysis was conducted to identify and quantify the metal nanoparticles (Table S2). Based on ICP-MS results, over 90% of Fe (14.9674 ppm) and W (11.5128 ppm)

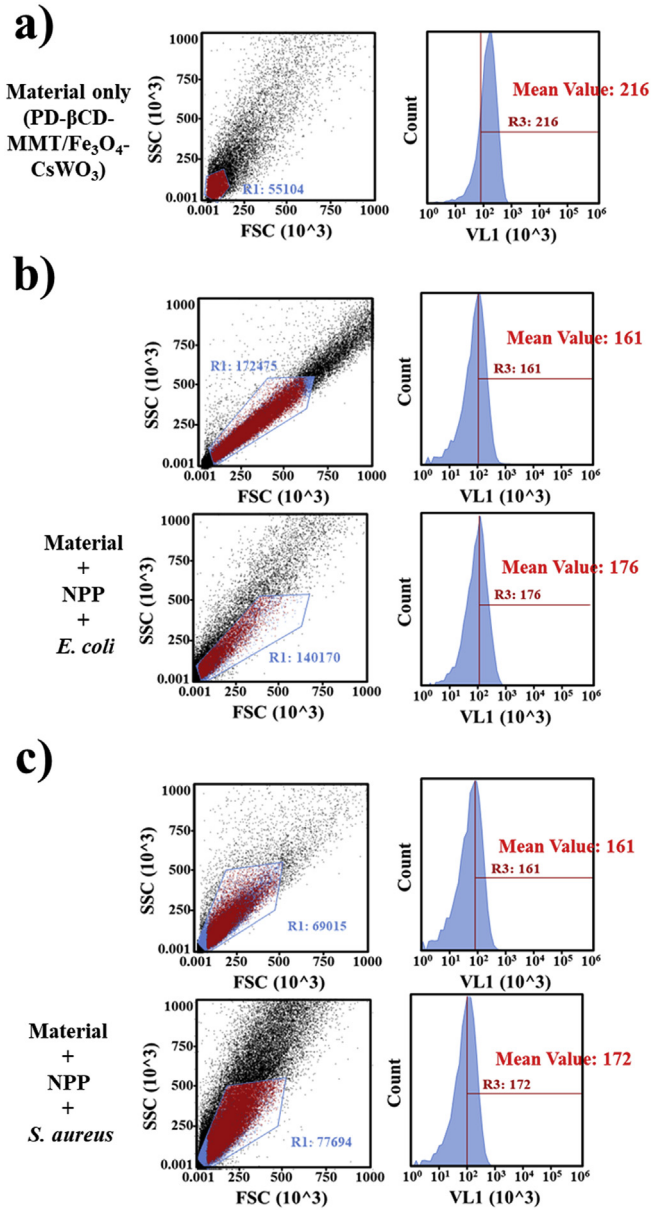

Fig. 5. Flow cytometry analysis of (a) PD-βCD-MMT/Fe_3O_4–$CsWO_3$ (0.1 mg/mL) and (b,c) PD-βCD-MMT/Fe_3O_4–$CsWO_3$ (0.1 mg/mL) in the presence of bacteria (10^7 CFU/mL).

were detected in the nanocomposite after recycling 4 times, confirming the stability of Fe_3O_4 and $CsWO_3$ in PD-βCD-MMT/Fe_3O_4–$CsWO_3$ after several usages on bacteria. Furthermore, fluorescence recovery using pH shock and new β-CD addition, after recycling, was observed using a PL spectrometer. The fluorescence intensity of PD-βCD-MMT/Fe_3O_4–$CsWO_3$ which was quenched following bacterial detection, recovered when pH shock was applied. The pH shock (pH 6 or below) may cause fluorescence recovery in material by triggering the cleavage of the diol-diol bond between boronic acid and β-CD, which results in the release of NP-loaded β-CD. To make the material further useable for detecting bacteria, new β-CD molecules were re-conjugated onto the nanocomposite. XRD analysis showed that the β-CD peak at 2θ of 11°-12° disappeared after pH shock and re-appeared after re-conjugation, indicating that following pH shock, β-CD was released from material due to cleavage of the diol-diol bond between boronic acid

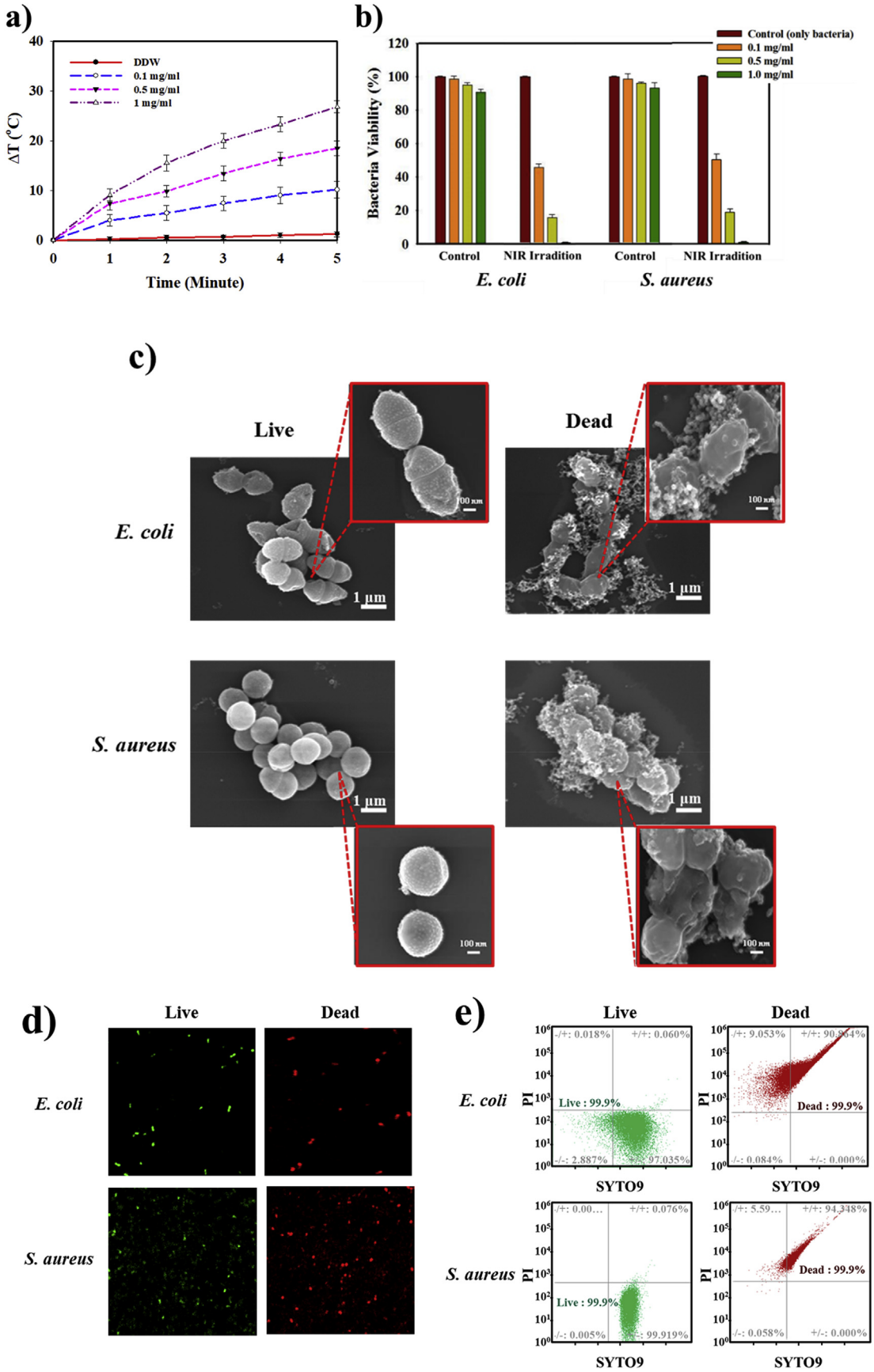

Fig. 6. (a) Photothermal effect of PD-βCD-MMT/Fe_3O_4–$CsWO_3$, and (b) Bacterial viability in the presence of various PD-βCD-MMT/Fe_3O_4–$CsWO_3$ concentration with and without (control) 5 min NIR irradiation (808 nm laser irradiation, power density 2 W/cm^2). (c) SEM images, (d) confocal images, and (e) flow cytometry analysis of live and dead bacteria after 5 min NIR irradiation in the presence of PD-βCD-MMT/Fe_3O_4–$CsWO_3$. A SYTO 9 (live) and PI staining (dead) was used for confocal and flow cytometry analysis.

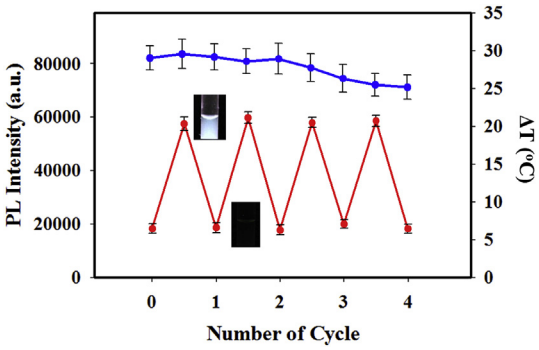

Fig. 7. Photothermal effects and PL intensity of PD-βCD-MMT/Fe_3O_4–$CsWO_3$ (1 mg/mL) after 4 times of recycling.

and β-CD, and the new β-CD molecules were successfully conjugated with the remaining boronic acid in the material (Fig. S13). These results confirmed that PD-βCD-MMT/Fe_3O_4–$CsWO_3$ offer an effective, efficient, and reusable approach for detecting and killing bacteria, based on ALP activity and the photothermal effect of $CsWO_3$ under NIR irradiation.

4. Conclusion

The reusable ALP-sensitive and NIR-responsive PD-βCD-MMT/Fe_3O_4–$CsWO_3$, meant for simultaneous detection and eradication of bacteria, was prepared by intercalating ALP-sensitive PD onto MMT clay *via* an ionic exchange reaction, followed by immobilization of Fe_3O_4 and $CsWO_3$ nanoparticles *via* metal-catechol interaction. The ability to detect bacteria relied on the enzymatic reaction of ALP, which hydrolyzed phosphate substrates and caused quenching of ALP-sensitive PD. The PD-βCD-MMT/Fe_3O_4–$CsWO_3$ showed strong fluorescence intensity, which was quenched when ALP (0–1000 U/L) hydrolyzed NPP into NP at the hydrophobic site of β-CD, which, in turn, led to the PET phenomenon. The fluorescence intensity of PD-βCD-MMT/Fe_3O_4–$CsWO_3$ was quenched in the presence of both *E. coli* and *S. aureus* (10^1–10^7 CFU/mL), indicating a good ability to detect bacteria. Furthermore, PD-βCD-MMT/Fe_3O_4–$CsWO_3$ also displayed high antibacterial activity against *E. coli* and *S. aureus* under NIR irradiation due to the generation of photothermal heat, leading to photothermolysis of bacterial cells, with the colorimetric detection capability remaining stable even after 4 recycles. Thus, this ALP-sensitive and NIR-responsive nanocomposite shows potential for simultaneous detection and eradication of bacteria, with recyclability which is simple, rapid, and effective.

Declaration of interest

None.

Acknowledgements

This research was supported by the Basic Science Research Program through the National Research Foundation of Korea (NRF) funded by the Ministry of Education (NRF-2017R1A2B2002365 and 2018R1A6A1A03023788).

Appendix A. Supplementary data

Supplementary data to this article can be found online at https://doi.org/10.1016/j.aca.2019.07.053.

References

[1] M. Majdinasab, A. Hayat, J.L. Marty, Aptamer-based assays and aptasensors for detection of pathogenic bacteria in food samples, TrAC Trends Anal. Chem. (Reference Ed.) 107 (2018) 60–77, https://doi.org/10.1016/j.trac.2018.07.016.
[2] S.G. Roh, A.I. Robby, P.T.M. Phuong, I. In, S.Y. Park, Photoluminescence-tunable fluorescent carbon dots-deposited silver nanoparticle for detection and killing of bacteria, Mater. Sci. Eng. C 97 (2019) 613–623, https://doi.org/10.1016/j.msec.2018.12.070.
[3] M.I. Azzam, S.M. Ezzat, B.A. Othman, K.A. El-Dougdoug, Antibiotics resistance phenomenon and virulence ability in bacteria from water environment, Water Sci. 31 (2017) 109–121, https://doi.org/10.1016/j.wsj.2017.10.001.
[4] H. Liu, X. Zhang, H. Zhang, X. Yao, M. Zhou, J. Wang, Z. He, H. Zhang, L. Lou, W. Mao, P. Zheng, B. Hu, Effect of air pollution on the total bacteria and pathogenic bacteria in different sizes of particulate matter, Environ. Pollut. 233 (2018) 483–493, https://doi.org/10.1016/j.envpol.2017.10.070.
[5] J. Heo, S.Z. Hua, An overview of recent strategies in pathogen sensing, Sensors (Switzerland) 9 (2009) 4483–4502, https://doi.org/10.3390/s90604483.
[6] O. Lazcka, F.J. Del Campo, F.X. Muñoz, Pathogen detection: a perspective of traditional methods and biosensors, Biosens. Bioelectron. 22 (2007) 1205–1217, https://doi.org/10.1016/j.bios.2006.06.036.
[7] E.B. Kang, Z.A.I. Mazrad, A.I. Robby, I. In, S.Y. Park, Alkaline phosphatase-responsive fluorescent polymer probe coated surface for colorimetric bacteria detection, Eur. Polym. J. 105 (2018) 217–225, https://doi.org/10.1016/j.eurpolymj.2018.05.035.
[8] A. Ahmed, J.V. Rushworth, N.A. Hirst, P.A. Millner, Biosensors for whole-cell bacterial detection, Clin. Microbiol. Rev. 27 (2014) 631–646, https://doi.org/10.1128/CMR.00120-13.
[9] A.I. Mazrad Zihnil, I. In, S.Y. Park, Reusable Fe_3O_4 and WO_3 immobilized onto montmorillonite as a photo-reactive antimicrobial agent, RSC Adv. 6 (2016) 54486–54494, https://doi.org/10.1039/c6ra08180k.
[10] C.Y. Shi, N. Deng, J.J. Liang, K.N. Zhou, Q.Q. Fu, Y. Tang, A fluorescent polymer dots positive readout fluorescent quenching lateral flow sensor for ractopamine rapid detection, Anal. Chim. Acta 854 (2015) 202–208, https://doi.org/10.1016/j.aca.2014.11.005.
[11] L. Mao, M. Gao, X. Xue, L. Yao, W. Wen, X. Zhang, S. Wang, Organic-inorganic nanoparticles molecularly imprinted photoelectrochemical sensor for α-solanine based on p-type polymer dots and n-CdS heterojunction, Anal. Chim. Acta 1059 (2019) 94–102, https://doi.org/10.1016/j.aca.2019.01.039.
[12] Y.K. Kim, J.E. Lee, B. Ryplida, C.A. Choi, Z.A.I. Mazrad, G. Lee, S. Lee, I. In, J.H. Jeong, S.Y. Park, Redox-responsive FRET-based polymer dot with BODIPY for fluorescence imaging-guided chemotherapy of tumor, Eur. J. Pharm. Biopharm. 132 (2018) 200–210, https://doi.org/10.1016/j.ejpb.2018.09.025.
[13] K.J. Cheng, J.W. Costerton, Alkaline phosphatase activity of rumen bacteria, Appl. Environ. Microbiol. 5 (1977) 586–590.
[14] K. Hatayama, Y. Nishihara, S. Kimura, K. Goto, D. Nakamura, A. Wakita, Y. Urasoko, Serum alkaline phosphatase isoenzymes in laboratory beagle dogs detected by polyacrylamide-gel disk electrophoresis, J. Toxicol. Sci. 36 (2011) 653–660, doi:JST.JSTAGE/jts/36.653 [pii].
[15] N.J. Fernandez, B.A. Kidney, Alkaline phosphatase: beyond the liver, Vet. Clin. Pathol. 36 (2007) 223–227, https://doi.org/10.1111/j.1939-165X.2007.tb00216.x.
[16] J.L. Millán, Alkaline Phosphatases : structure, substrate specificity and functional relatedness to other members of a large superfamily of enzymes, Purinergic Signal. 2 (2006) 335–341, https://doi.org/10.1007/s11302-005-5435-6.
[17] B.F. Favarin, M.A.R. Andrade, M. Bolean, A.M.S. Simão, A.P. Ramos, M.F. Hoylaerts, J.L. Millán, P. Ciancaglini, Effect of the presence of cholesterol in the interfacial microenvironment on the modulation of the alkaline phosphatase activity during in vitro mineralization, Colloids Surfaces B Biointerfaces 155 (2017) 466–476, https://doi.org/10.1016/j.colsurfb.2017.04.051.
[18] I. Roman, R.D. Trusca, M.-L. Soare, C. Fratila, E. Krasicka-Cydzik, M.-S. Stan, A. Dinischiotu, Titanium dioxide nanotube films Preparation, characterization and electrochemical biosensitivity towards alkaline phosphatase, Mater. Sci. Eng. C 37 (2014) 374–382, https://doi.org/10.1016/j.msec.2014.01.036.
[19] M. Lai, Z. Jin, W. Qiao, Surface immobilization of gelatin onto TiO_2 nanotubes to modulate osteoblast behavior, Colloids Surfaces B Biointerfaces 159 (2017) 743–749, https://doi.org/10.1016/j.colsurfb.2017.08.043.
[20] P. Gettins, M. Metzler, J.E. Coleman, Alkaline phosphatase. ^{31}P NMR probes of the mechanism, J. Biol. Chem. 260 (1985) 2875–2883.
[21] N.S. Terefe, J.M. Arimi, A. Van Loey, M. Hendrickx, Kinetics of the alkaline phosphatase catalyzed hydrolysis of disodium p-nitrophenyl phosphate: effects of carbohydrate additives, low temperature, and freezing, Biotechnol. Prog. 20 (2004) 1467–1478, https://doi.org/10.1021/bp0498894.
[22] H. Liu, M. Li, Y. Xia, X. Ren, A turn-on fluorescent sensor for selective and sensitive detection of alkaline phosphatase activity with gold nanoclusters based on inner filter effect, ACS Appl. Mater. Interfaces 9 (2017) 120–126, https://doi.org/10.1021/acsami.6b11920.
[23] M.I. Halawa, W. Gao, M. Saqib, S.A. Kitte, F. Wu, G. Xu, Sensitive detection of alkaline phosphatase by switching on gold nanoclusters fluorescence quenched by pyridoxal phosphate, Biosens. Bioelectron 95 (2017) 8–14, https://doi.org/10.1016/j.bios.2017.03.073.
[24] Z. Song, R.T.K. Kwok, E. Zhao, Z. He, Y. Hong, J.W.Y. Lam, B. Liu, B.Z. Tang, A ratiometric fluorescent probe based on ESIPT and AIE processes for alkaline phosphatase activity assay and visualization in living cells, ACS Appl. Mater.

Interfaces 6 (2014) 17245–17254, https://doi.org/10.1021/am505150d.
[25] S.-J. Li, C.-Y. Li, Y.-F. Li, J. Fei, P. Wu, B. Yang, J. Ou-Yang, S.-X. Nie, Facile and sensitive near-infrared fluorescence probe for the detection of endogenous alkaline phosphatase activity in vivo, Anal. Chem. 89 (2017) 6854–6860, https://doi.org/10.1021/acs.analchem.7b01351.
[26] L. Jia, J.-P. Xu, D. Li, S.-P. Pang, Y. Fang, Z.-G. Song, J. Ji, Fluorescence detection of alkaline phosphatase activity with β-cyclodextrin-modified quantum dots, Chem. Commun. (Camb). 46 (2010) 7166–7168, https://doi.org/10.1039/c0cc01244k.
[27] E.B. Kang, C.A. Choi, Z.A.I. Mazrad, S.H. Kim, I. In, S.Y. Park, Determination of cancer cell-based pH-sensitive fluorescent carbon nanoparticles of cross-linked polydopamine by fluorescence sensing of alkaline phosphatase activity on coated surfaces and aqueous solution, Anal. Chem. 89 (2017) 13508–13517, https://doi.org/10.1021/acs.analchem.7b03853.
[28] S.J. Park, E.B. Kang, S.M. Sharker, G. Lee, I. In, S.Y. Park, NIR-mediated antibacterial clay nanocomposites: exfoliation of montmorillonite nanolayers by IR825 intercalation, Macromol. Mater. Eng. 301 (2016) 141–148, https://doi.org/10.1002/mame.201500272.
[29] C.J. Jeong, E.B. Kang, S.J. Park, K.H. Choi, G. Shin, I. In, S.Y. Park, Preparation of exfoliated montmorillonite nanocomposites with catechol/zwitterionic quaternized polymer for an antifouling coating, Polym. Eng. Sci. 55 (2015) 2111–2117, https://doi.org/10.1002/pen.24052.
[30] J.Y. Kim, S.Y. Jeong, G.J. Shin, S.K. Lee, K.H. Choi, Near infrared cut-off characteristics of various perovskite-based composite films, Appl. Mech. Mater. 229–231 (2012) 2733–2736, https://doi.org/10.4028/www.scientific.net/amm.229-231.2733.
[31] J.A. Nam, A. Al Nahain, S.M. Kim, I. In, S.Y. Park, Successful stabilization of functionalized hybrid graphene for high-performance antimicrobial activity, Acta Biomater. 9 (2013) 7996–8003, https://doi.org/10.1016/j.actbio.2013.04.022.
[32] C.A. Choi, J.E. Lee, Z.A.I. Mazrad, I. In, J.H. Jeong, S.Y. Park, Redox- and pH-responsive fluorescent carbon nanoparticles-MnO_2-based FRET system for tumor-targeted drug delivery *in vivo* and *in vitro*, J. Ind. Eng. Chem. 63 (2018) 208–219, https://doi.org/10.1016/j.jiec.2018.02.017.
[33] M. Lai, P. Liu, H. Lin, Y. Luo, H. Li, X. Wang, R. Sun, Interaction between chitosan-based clay nanocomposites and cellulose in a chemical pulp suspension, Carbohydr. Polym. 137 (2016) 375–381, https://doi.org/10.1016/j.carbpol.2015.10.099.
[34] G.B.B. Varadwaj, S. Rana, K.M. Parida, A stable amine functionalized montmorillonite supported Cu, Ni catalyst showing synergistic and co-operative effectiveness towards C-S coupling reactions, RSC Adv. 3 (2013) 7570–7578, https://doi.org/10.1039/c3ra40183a.
[35] S.M. Sharker, S.M. Kim, S.H. Kim, I. In, H. Lee, S.Y. Park, Target delivery of β-cyclodextrin/paclitaxel complexed fluorescent carbon nanoparticles: externally NIR light and internally pH sensitive-mediated release of paclitaxel with bio-imaging, J. Mater. Chem. B. 3 (2015) 5833–5841, https://doi.org/10.1039/c5tb00779h.
[36] E.B. Kang, I. In, K.D. Lee, S.Y. Park, Mitochondria-targeted fluorescent carbon nano-platform for NIR-triggered hyperthermia and mitochondrial inhibition, J. Ind. Eng. Chem. 55 (2017) 224–233, https://doi.org/10.1016/j.jiec.2017.06.053.
[37] C. Li, Y. Zhu, X. Zhang, X. Yang, C. Li, Metal-enhanced fluorescence of carbon dots adsorbed Ag@SiO_2 core-shell nanoparticles, RSC Adv. 2 (2012) 1765–1768, https://doi.org/10.1039/c2ra01032a.
[38] Y. Zhang, H. Gonalves, J.C.G. Esteves Da Silva, C.D. Geddes, Metal-enhanced photoluminescence from carbon nanodots, Chem. Commun. 47 (2011) 5313–5315, https://doi.org/10.1039/c0cc03832f.
[39] K. Manthiram, A.P. Alivisatos, Tunable localized surface plasmon resonances in tungsten oxide nanocrystals, J. Am. Chem. Soc. 134 (2012) 3995–3998, https://doi.org/10.1021/ja211363w.
[40] V.K. Gasparyan, I.L. Bazukyan, Lectin sensitized anisotropic silver nanoparticles for detection of some bacteria, Anal. Chim. Acta 766 (2013) 83–87, https://doi.org/10.1016/j.aca.2012.12.015.
[41] N. Massad-Ivanir, G. Shtenberg, A. Tzur, M.A. Krepker, E. Segal, Engineering nanostructured porous SiO_2 surfaces for bacteria detection via "direct cell capture,", Anal. Chem. 83 (2011) 3282–3289, https://doi.org/10.1021/ac200407w.
[42] S.H. Ohk, A.K. Bhunia, Multiplex fiber optic biosensor for detection of Listeria monocytogenes, Escherichia coli O157:H7 and Salmonella enterica from ready-to-eat meat samples, Food Microbiol. 33 (2013) 166–171, https://doi.org/10.1016/j.fm.2012.09.013.
[43] Y. Wang, W. Knoll, J. Dostalek, Bacterial pathogen surface plasmon resonance biosensor advanced by long range surface plasmons and magnetic nanoparticle assays, Anal. Chem. 84 (2012) 8345–8350, https://doi.org/10.1021/ac301904x.
[44] F. Mouffouk, A.M. Rosa da Costa, J. Martins, M. Zourob, K.M. Abu-Salah, S.A. Alrokayan, Development of a highly sensitive bacteria detection assay using fluorescent pH-responsive polymeric micelles, Biosens. Bioelectron. 26 (2011) 3517–3523, https://doi.org/10.1016/j.bios.2011.01.037.
[45] C.F. Fronczek, D.J. You, J.Y. Yoon, Single-pipetting microfluidic assay device for rapid detection of Salmonella from poultry package, Biosens. Bioelectron. 40 (2013) 342–349, https://doi.org/10.1016/j.bios.2012.07.076.
[46] F. Illien, N. Rodriguez, M. Amoura, A. Joliot, M. Pallerla, S. Cribier, F. Burlina, S. Sagan, Quantitative fluorescence spectroscopy and flow cytometry analyses of cell-penetrating peptides internalization pathways: optimization, pitfalls, comparison with mass spectrometry quantification, Sci. Rep. 6 (2016) 36938, https://doi.org/10.1038/srep36938.
[47] S.K. Boda, K. Ravikumar, D.K. Saini, B. Basu, Differential viability response of prokaryotes and eukaryotes to high strength pulsed magnetic stimuli, Bioelectrochemistry 106 (2015) 276–289, https://doi.org/10.1016/j.bioelechem.2015.07.009.